Understanding Proton Introduction and Migration in Yttria-Stabilized Zirconia from DFT Calculations and Muon-Spin Spectroscopy

A. G. Marinopoulos[1*], R. C. Vilão[1], H. V. Alberto[1], J. M. Gil[1], R. B. L. Vieira[2] and J. S. Lord[3]

[1] *CFisUC, Department of Physics, University of Coimbra, Coimbra, Portugal*
[2] *CICECO - Aveiro Institute of Materials, Department of Chemistry, University of Aveiro, Portugal*
[3] *ISIS Facility, Rutherford Appleton Laboratory, Chilton, Didcot, UK*
*Corresponding author: marinop@uc.pt

Received 19/03/2024; accepted 01/09/2024
https://doi.org/10.4152/pea.2026440205

Abstract
YSZ is a compound with an important role in electrochemistry applications, due to its high electrical conductivity. It is commonly used as electrolyte in solid-oxide fuel cells. Several studies have also suggested additional uses of this material as a proton conductor, when grown in Nc form. The present research reports combined theoretical and experimental results that examined the incorporation and properties of proton defect in YSZ. The calculations were based on DFT and NEB methods. MSS was also performed by studying muons evolution, a lighter hydrogen particle with non-zero spin. The results provided vital information on the formation energetics of proton defect, its migration behavior and electronic structure.

Keywords: DFT; MSS; NEB; YSZ.

Introduction•

Cubic YSZ is a wide-gap ceramic with diverse uses in many technologically important applications [1]. In the field of electrochemistry, YSZ is commonly employed as electrolyte material in solid-oxide fuel cells [2]. It is an ionic conductor with electrical conductivity mediated by the diffusion of oxygen ions. Proton incorporation in bulk YSZ has been studied in the pioneering work of Wagner, where the solubility of protons in YSZ solutions was found to be low [3, 4].
However, recent studies have reported high levels of electrical power originating from proton conduction in monocrystalline Nc-YSZ samples, at T below 150 ºC [5-7]. An explanation for these findings is linked to a numbers of issues: a) How easy it is for protons to dissolve in bulk YSZ lattice?; b) What are the mechanisms of proton diffusion and associated migration-energy barriers?; and c) Does proton diffusion in Nc-YSZ take place through the bulk or through fast-diffusion pathways such as grain boundaries or internal surfaces?

• The abbreviations list is in page 149.

The present work reviews and discusses some of its authors' recent combined theoretical and experimental works on hydrogen defects in cubic YSZ [8-12]. The calculations were based on DFT theory [13, 14], under generalized-gradient approximation for exchange and correlation effects. They were carried out to determine the formation energy and migration behavior of protons in YSZ lattice. Experimentally, results of MSS experiments, where the implantation and evolution of muons, a much lighter hydrogen particle [15], were monitored and analyzed, are also herein presented.

Theoretical preliminaries

First-principles calculations based on DFT theory were performed with the aid of *Vienna Ab initio* Simulation Package computational code [16-18]. A plane-wave basis limited by a cut-off energy of 420 eV was taken for the expansion of crystalline valence-electron wave functions. Pseudopotentials based on projector-augmented wave method [19] were used to represent valence-core interaction. Exchange and correlation effects between electrons were described within generalized-gradient approximation and PBE semi-local functional [20]. Minimum-energy paths and migration barriers of proton diffusion were determined by NEB method [21], through the creation of intermediate system replicas connecting initial and final proton configurations in YSZ structure.

Structurally, YSZ lattice was represented by quasi-random bulk cubic-zirconia supercells where yttria formula units were added to achieve a stoichiometry of a10.3 mol% YSZ solution, which is within the stability limits of cubic phase [8]. Yttrium atoms were introduced in the cation sublattice of zirconia, according to the following reaction, expressed in Kröger-Vink notation:

$$Y_2O_3 \rightarrow 2Y'_{Zr} + v_O^{\cdot\cdot} + 3O_O^{\times} \quad (1)$$

Negatively-charged Y_{Zr} defects are charge compensated by the creation of doubly positively charged oxygen vacancies, υ_0, in order to achieve overall charge neutrality. $O_O^{\times}$ denotes oxygen atoms at their normal lattice sites.

Defect-formation energies

Hydrogen atoms were inserted interstitially inside YSZ supercell, at various locations. Minimum-energy equilibrium sites were determined for each charge state of hydrogen by energy minimization. Final formation energies were determined as a function of Fermi energy, E_F, within YSZ band gap, according to the following expression:

$$\Delta E_{def}^{form} = E_{def}^{tot} - E_{bulk}^{tot} + (\Delta n)\mu_H + q(E_F + E_V) \quad (2)$$

where E_{def}^{tot} and E_{bulk}^{tot} represent the defect's total energies (within embedded hydrogen atom) and pristine bulk-lattice supercells, respectively; μ_H denotes the magnitude of hydrogen chemical potential; Δn accounts for deviations from stoichiometry; q is defect charge state; and E_V stands for the value of valence-band edge, which served as reference energy for Fermi level. Band gap of 3.91 eV was obtained from DFT-PBE, a value that underestimated YSZ experimental gap [8].

Final formation energies for different charge states of hydrogen are shown in Fig. 1, as a function of Fermi level in the gap. It can be seen that neutral state is never thermodynamically stable for any position of Fermi level. Instead, monatomic hydrogen is an amphoteric defect in YSZ, with pinning level (+/-) at 1.47 eV below conduction band edge, E_C. In band gap largest part, hydrogen is positively charged; thus, it is thermodynamically stable as a proton defect: H^+. In Fig. 1, Fermi-level energies ranged from zero (valence-band edge, E_V) to E_C.

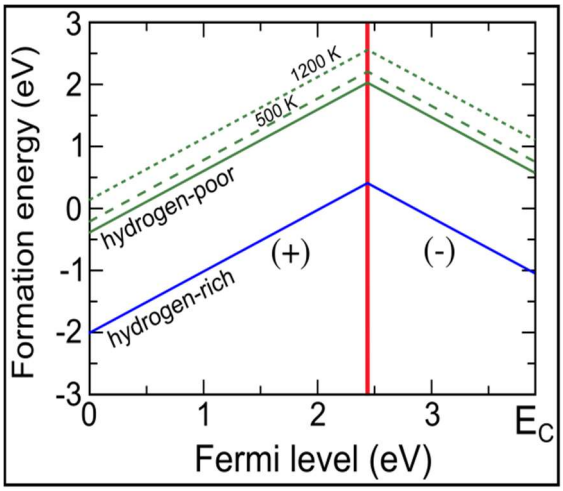

Figure 1: Formation energy of interstitial hydrogen in YSZ for hydrogen-rich and hydrogen-poor conditions as a function of Fermi-level position inside band gap. The red vertical line denotes (+/-) pinning level.

The dependence of formation energies on specific value of hydrogen chemical potential is depicted in Fig. 1. For hydrogen-rich conditions (equilibrium with hydrogen gas, H_2(g)) corresponding formation energy is lower. Nonetheless, hydrogen-poorest conditions are the most realistic conditions in practical applications where YSZ samples are in equilibrium with a surrounding water vapor, H_2O(g). In this case, formation energies were higher, and hydrogen chemical potential is given as:

$$\mu_H = \frac{1}{2}(\mu^o_{H_2O} - \mu^o_O) \quad (3)$$

where $\mu^o_{H_2O}$ are μ^o_O are chemical potentials of water and oxygen, respectively, in their respective gas states, at standard T and partial-pressure conditions.
Furthermore, assuming an ideal-gas behavior for gas phases, effects of T and partial pressure can also be included to chemical potentials, as follows:

$$\mu(T,p) = \mu^o + \Delta\mu(T,p^o) + k_B T ln(\frac{p}{p^o}) \quad (4)$$

where μ^o denotes hydrogen chemical potential at standard conditions of T = 298.15 K and p^o = 1 atm. $\Delta\mu(T, p^o)$ is T-dependent part of chemical potential. These quantities were obtained from thermochemical tables [22].

Structurally, it was observed that H^+ bound to oxygen ions, forming hydroxyl-type O-H bonds, with bond lengths within a very narrow range, from 0.98 to 1.00 Å. Due to the disordered structure of YSZ lattice, H^+ binding to various O ions led to not iso-energetic configurations [12]. In fact, lower formation energies were recorded for O-H configurations very near oxygen vacancies (see Fig. 2a).
These results suggest that intrinsic oxygen vacancies of YSZ lattice defined trapping regions within YSZ, where protons preferably bind with oxygen ions which were the nearest neighbors of these vacancies. The structural relaxation pattern shows that O-H hydroxyl bond was accommodated by a breaking of one (or two) Zr-O host bonds, rendering participating O ion under-coordinated (see Fig. 2b).

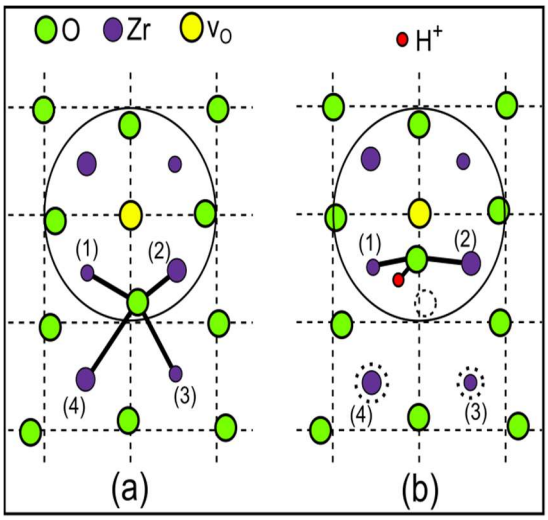

Figure 2: (a) YSZ lattice near an oxygen vacancy. **(b)** Proton configuration in YSZ lattice- formation of dative O-H bond and breaking of two Zr-O host bonds.

After establishing equilibrium sites and formation energies of protons in YSZ lattice, the next step was to determine energy balance of hydration reaction. Accordingly, protons incorporated into bulk YSZ lattice through dissociative dissolution of water molecules from surrounding atmosphere. Hydration reaction can be expressed as:

$$H_2O(g) + v_O^{\cdot\cdot} + O_O^{\times} \Leftrightarrow 2OH_O^{\cdot} \qquad (5)$$

A water molecule transferred from gas phase was the source of two protons that entered the oxide lattice, and oxygen atom filled an oxygen vacancy. Hydration enthalpy (T = 0 K) of this reaction can be obtained as follows:

$$\Delta E_{hydr}^{tot} = 2\Delta E_{OH_O^{\cdot}}^{form} - \Delta E_{v_O^{\cdot\cdot}}^{form} \qquad (6)$$

Considering formation energy of proton defect (see Fig. 1) and of the doubly positively charged oxygen vacancy [12], net balance of hydration reaction was negative (13 eV). Thus, hydration was an exothermic process and YSZ lattice favorably accommodated proton defects from surrounding water atmosphere, at low T.

Migration pathways and barriers

A number of migration pathways representing plausible possibilities for proton motion in entire YSZ lattice were considered. DFT calculations with NEB method identified two distinct groups of paths with substantially different migration barriers. Pathways spatially confined within the immediate neighborhood of individual oxygen vacancies were found to be short ranged (see Fig. 3), and to have low to moderate barriers ranging from 0.13 to 1.02 eV (Fig. 4).

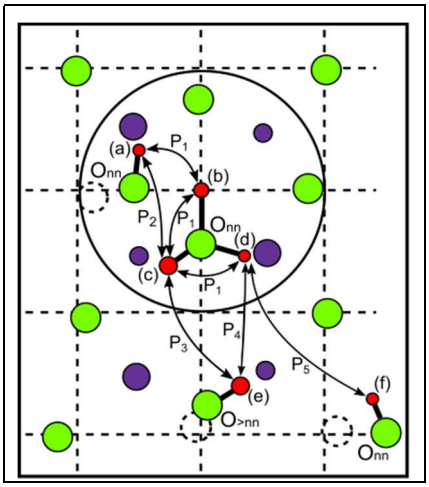

Figure 3: Migration paths of proton in YSZ lattice, denoted by arrows connecting initial and final proton sites. Oxygen vacancy site is represented by "b".

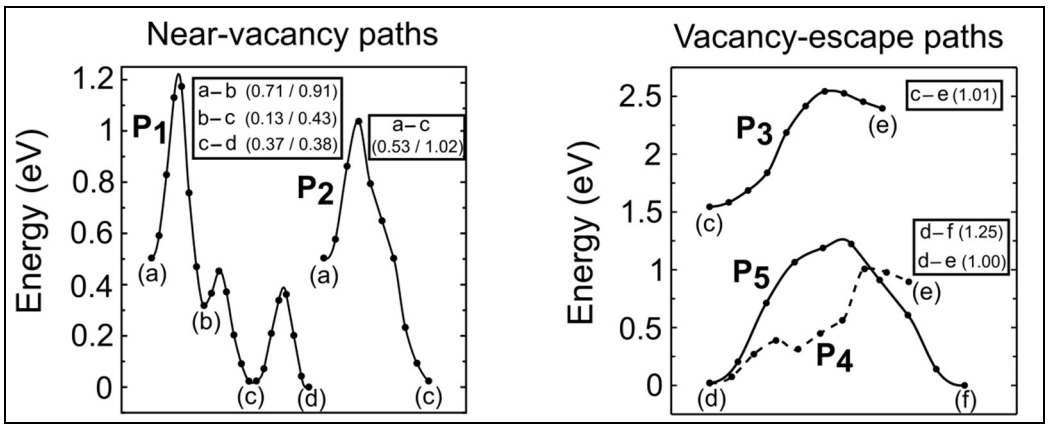

Figure 4: Energy profiles of proton migration paths depicted in Fig. 3. Energy barriers (in eV) for forward/backward motion are shown inside parentheses for specific migration segments.

These paths comprise both proton-transport and bond reorientation modes of migration. In contrast, vacancy escape paths are exclusively proton-transport type and have a longer range (Fig. 3). These paths should normally be linked to long-range macroscopic diffusion, and are associated with larger barriers, in excess of 1 eV (see Fig. 4). These findings strongly suggested that proton mobility in bulk YSZ should be rather low.

Additional NEB calculations were also performed for proton paths at the core of a high-angle grain boundary [12]. Such extended defects constitute an integral part of Nc-YSZ samples internal structure. Calculations showed that Zr-Zr cation stacking at the core of these interfaces acted as strong obstacle to proton motion, creating very high barriers to overcome. Therefore, it is quite doubtful that grain boundaries can be fast diffusion pathways for proton transport. The only alternative for the reported high protonic conductivity in Nc-YSZ appears to be that protonic defects diffuse unhindered along internal surfaces of Nc-YSZ samples [7]. This could be accomplished either by executing hopping jumps between oxygen ions as protons, or through a vehicle mechanism where H^+ ions are part of larger groups (for instance H_3O^+ ions) that are present from water dissolution to the surface from a wet atmosphere.

MSS

MSS has become a standard technique for studying monatomic hydrogen configurations through modelling with muonium, a light pseudo isotope where the hydrogenic atom possesses a positive muon as nucleus: μ^+-e^- [23, 24]. Although the muon is only one-ninth the proton mass, muonium reduced mass 99.6% that of hydrogen, so that the respective electronic properties should be nearly identical [25, 26]. MSS has also the additional advantage of being restricted to high-dilution limit for muonium impurity, which can thus generally be regarded as isolated, only indirectly affected by other defects or impurities through overall Fermi energy.

MSS experiments took place at EMU instrument of ISIS Facility, Rutherford Appleton Laboratory, UK. A Nc YSZ ($Zr_{0.92}Y_{0.08}O_2$) sample (grain size 13 nm) provided by Innovnano was investigated. In the experiments, 4 MeV positive muons were implanted into the sample. In the first one, a magnetic field (B = 10 mT) was applied perpendicularly to initial MSS polarization, at T of 8.5 K. Fig. 5 shows a Fourier transform of obtained MSS high statistics (using Lomb method [27]): the level of probability of false alarm below 0.0001 is shown as a pointed line in Fig. 5.

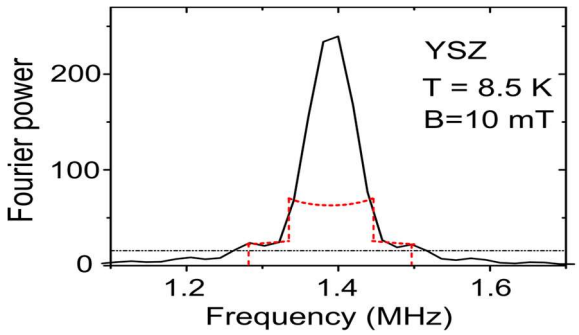

Figure 5: μSRS Fourier spectrum of YSZ at T = 8.5 K in an external magnetic field of B = 10 mT. The red dashed line is a simulation of a powder spectrum with A_{iso} = 0 MHz and D = 0.2 MHz.

The results clearly indicate, as identified previously [11], that MSS signal basically corresponds to positively-charged muons precessing at Larmor frequency. However, the frequency line width clearly exceeds the one expected from nuclear

dipolar broadening, which indicates the presence of a small electronic spin density at the muon. Similar results have been obtained in other oxide systems [28], revealing that hyperfine interaction was mainly dipolar. One may immediately estimate its approximate value from the full width at line half maximum, which yields a dipolar term: $D \approx \lambda/\pi = 0.11$ MHz. A closer inspection of Fig. 5 reveals the existence of a small spectral power above the threshold for false alarm, at frequencies of f1 ≈ 1.3 MHz and f2 ≈ 1.5 MHz. These are likely to correspond to expected steps of a powder-pattern hyperfine spectrum [29]. Powder pattern represented as a red dashed line in Fig. 5 is a simulation with the model of [29], using a value of isotropic hyperfine interaction $A_{iso} = 0$, and D corresponds approxim. to $D \approx f2 - f1 = 0.2$ MHz. Both approaches indicate that hyperfine interaction was of almost pure dipolar origin ($A_{iso} \approx 0$ and with D ≈ 0.1 MHz- at most, 0.2 MHz).

A notable feature is that a significant part of MSS polarization was not seen at low T (missing fraction) [11]. The missing fraction is related to muons depolarizing rapidly during thermalization stage, due to the formation of deeply bound muonium. Thus, one assigns the missing fraction to muons thermalizing in interstitial configurations [8] (either pure interstitial or oxygen-vacancy site). Nevertheless, hyperfine interaction associated to these configurations can be characterized by means of longitudinal-field repolarization technique. Fig. 6 shows repolarization curve for YSZ, at T = 300 K. This curve is two-stepped, which is a usual sign of anisotropy [30]. Therefore, the data were fitted (Fig. 6) with phenomenological repolarization functions proposed in [30]. Obtained values were $A_{iso} = 2.1(2)$ GHz and D = 0.13(2) GHz. The corresponding fit is shown as a red line in Fig. 6.

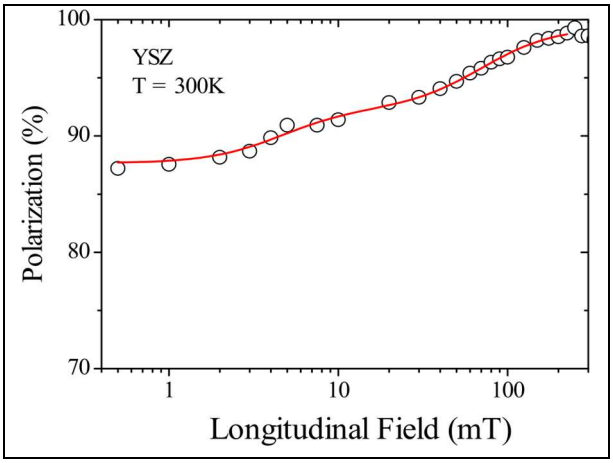

Figure 6: Repolarization curve for YSZ at T = 300 K. The red line is a fit assuming an axially symmetric anisotropic hyperfine interaction, as discussed in the text.

However, calculated hyperfine interaction for interstitial hydrogen in cubic bulk YSZ has been calculated in [10] as being essentially isotropic, with $A_{iso} \approx 3$ GHz. This value is much higher than $A_{iso} = 2.1(1)$ GHz, which is the present study's experimental value. However, one must take into account that the sample used in these experiments is Nc, with an average grain size of 13 nm, implying an

important role of the grain surface. MSS experiments in Nc II-VI semiconductors present strong evidence of surface states formation [31]. Segregation of impurities on the nanograins surface is also a well-known effect [32], which may be enhanced with decreasing grain size [33]. Moreover, the first-principles calculations of [10] showed that hydrogen at the grain boundary core was characterized by different A_{iso} values from those of hydrogen in bulk regions. In certain cases, the corresponding value was found to be lower by as much as 20%. This finding was attributed to the distinct interface structure of the grain boundary. This could allow (in certain cases) a much larger spilling of valence electron density to neighboring ions, thus leading to a reduction of spin density at hydrogen nucleus and, consequently, to a smaller A_{iso} value for hydrogen, at the grain boundary core. The corresponding reduced values for muonium, after scaling took into account the 3.183 factor of magnetic moment ratio of the muon and the proton, were around $A_{iso} \approx 2.3$ GHz, which compared well with the experimental value. Therefore, it is probable that anisotropic component seen in Fig.6 corresponds to muonium influenced by the grains surface.

Conclusion

The proton defect in YSZ was studied by a combination of first-principles calculations and MSS measurements. By means of DFT calculations, the formation and hydration energies of protons in YSZ lattice were obtained, providing essential information on their local environment, thermodynamic stability and ease of incorporation from the water vapor. Representative migration pathways for protons were also identified linking the magnitude of diffusion barriers with YSZ internal microstructure. MSS allowed the characterization of hydrogen configurations in YSZ: an oxygen-bound configuration with a reduced electron spin density (with a mostly dipolar character) and an interstitial configuration with a high spin density. However, the latter was found to be much reduced with respect to theoretical estimates, indicating possible surface effects due to the nanometric size of crystalline grains.

Acknowledgements

This work was supported by FCT – *Fundação para a Ciência e Tecnologia, I. P.* (Portugal), projects UIDP/04564/2020 and UIDB/04564/2020. FCT is also acknowledged by R.B.L.V. for Researcher Positions (CEECIND/02127/2017). We acknowledge the use of the computing facilities of CFisUC of the University of Coimbra. We also acknowledge the ISIS Facility at the Rutherford Appleton Laboratory, UK, for beam time allocation and the technical help of the muon team.

Authors' contributions

A. G. Marinopoulos: draft preparation, project administration, investigation. **R. C. Vilão**: draft preparation, formal analysis, investigation. **H. V. Alberto**: review and editing. **J. M. Gil**: review and editing. **R. B. L. Vieira**: data curation, review and editing. **J. S. Lord**: data curation, review and editing.

Abbreviations

DFT: density-functional theory
MSS: Muon spin spectroscopy
Nc: Nanocrystalline
NEB: nudged elastic-band method
PBE: Perdew-Burke-Ernzerhof functional
T: temperature
YSZ: yttria-stabilized zirconia

References

1. Heuer A, Hobbs LW. Science and Technology of Zirconia. In: Adv Ceram. 3. The American Ceramic Society, Westerville, OH, 1981.
2. Badwal SPS. Zirconia-based solid electrolytes: microstructure, stability and ionic conductivity. Sol State Ion. 1992;52:23-32. https://doi.org/10.1016/0167-2738(92)90088-7
3. Wagner C. Die Löslichkeit von Wasserdampf in ZrO_2-Y_2O_3-Mischkristallen. Ber Bunsen Phys Chem. 1968;72:778-781. https://doi.org/10.1002/bbpc.19680720709;
4. Stotz S, Wagner C. Die Löslichkeit von Wasserdampf und Wasserstoff in festen Oxiden. Ber Bunsen Phys Chem. 1966;70:781-788. https://doi.org/10.1002/bbpc.19660700804
5. Chiodelli G, Maglia F, Anselmi-Tamburini U et al. Characterization of low temperature protonic conductivity in bulk nanocrystalline fully stabilized zirconia. Sol State Ion. 2009;180:297-301. https://doi.org/10.1016/j.ssi.2009.02.031
6. Avila-Paredes HJ, Zhao J, Wang S et al. Protonic conductivity of nano-structured Yttria-stabilized zirconia: dependence on grain size. J Mater Chem. 2010;20:990-994. https://doi.org/10.1039/b919100c
7. Scherrer B, Schlupp MVF, Stender D et al. On Proton Conductivity in Porous and Dense Yttria Stabilized Zirconia at Low Temperature. Adv Funct Mater. 2013;23:1957-1964. https://doi.org/10.1002/adfm.201202020
8. Marinopoulos AG. Incorporation and migration of hydrogen in yttria-stabilized cubic zirconia: Insights from semilocal and hybrid-functional calculations. Phys Rev B. 2012;86(15):155144. https://doi.org/10.1103/PhysRevB.86.155144
9. Vieira RBL, Vilão RC, Gordo PM et al. Muon-Spin-Rotation study of yttria-stabilized zirconia (ZrO^2:Y): Evidence for muon and electron separate traps. J Phys: Conf Ser. 2014;551:012050. https://doi.org/10.1088/1742-6596/551/1/012050
10. Marinopoulos AG. First-principles study of hydrogen configurations at the core of a high-angle grain boundary in cubic yttria-stabilized zirconia. J Phys: Condens Matter 2014;26(2):025502. https:/doi.org/10.1088/0953-8984/26/2/025502

11. Vieira RBL, Vilão RC, Marinopoulos AG et al. Isolated hydrogen configurations in zirconia as seen by muon spin spectroscopy and ab initio calculations. Phys Rev B. 2016;94(11):115207. https://doi.org/10.1103/PhysRevB.94.115207
12. Marinopoulos AG. Protons in cubic yttria-stabilized zirconia: Binding sites and migration pathways. Solid State Ion. 2018;315:116-125. https://doi.org/10.1016/j.ssi.2017.12.006
13. Hohenberg P, Kohn W. Inhomogeneous Electron Gas. Phys Rev. 1964;136:B864-B871. https://doi.org/10.1103/PhysRev.136.B864;
14. Kohn W, Sham LJ. Self-Consistent Equations Including Exchange and Correlation Effects. Phys Rev. 1965;140:A1133-A1138. https://doi.org/10.1103/PhysRev.140.A1133
15. Patterson B. Muonium states in semiconductors. Rev Mod Phys. 1988;60(1):69. https://doi.org/10.1103/RevModPhys.60.69
16. Kresse G, Hafner J. *Ab initio* molecular dynamics for liquid metals. Phys Rev B. 1993;47:558-561. https://doi.org/10.1103/PhysRevB.47.558;
17. Kresse G, Hafner J. *Ab initio* molecular-dynamics simulation of the liquid-metal-amorphous-semiconductor transition in germanium. Phys Rev B. 1994;49:14251-14269. https://doi.org/10.1103/PhysRevB.49.14251
18. Kresse G, Furthmüller J. Efficient iterative schemes for *ab initio* total-energy calculations using a plane-wave basis set. Phys Rev B. 1996;54:11169-11186. https://doi.org/10.1103/PhysRevB.54.11169
19. Blöchl PE. Projector augmented-wave method. Phys Rev B. 1994;50(24):17953-17979. https://doi.org/10.1103/PhysRevB.50.17953
20. Perdew JP, Burke K, Ernzerhof M. Generalized Gradient Approximation Made Simple. Phys Rev Lett. 1996;77:3865-3868. https://doi.org/10.1103/PhysRevLett.77.3865
21. Jónsson H, Mills G, Jacobsen KW et al. (Eds.). Nudged Elastic Band Method for Finding Minimum Energy Paths of Transitions, in: Classical and Quantum Dynamics in Condensed Phase Simulations. World Sci. 1998:385-404. https://doi.org/10.1142/9789812839664_0016
22. Chase MW Jr. NIST-JANAF Thermochemical Tables 4th Ed. American Chemical Society and American Institute of Physics for the National Institute of Standards and Technology. Woodbury NY, 1998.
23. Blundell SJ, De Renzi R, Lancaster T et al (Eds.). Muon Spectroscopy: An Introduction. Oxford University Press, Oxford, 2021. https://doi.org/10.1093/oso/9780198858959.001.0001
24. Hillier AD, Blundell SJ, McKenzie I et al. Muon spin spectroscopy. Nat Rev Meth Primer. 2022;2(1):4. https:/doi.org/10.1038/s43586-021-00089-0
25. Lichti RL, Chow KH, Gil JM et al. Location of the H[+/-] level: Experimental limits for muonium. Phys B. 2006;376-377:587-590. https://doi.org/10.1016/j.physb.2005.12.148
26. Cox SFJ, Lichti RL, Lord JS et al. The first 25 years of semiconductor muonics at ISIS, modelling the electrical activity of hydrogen in inorganic semiconductors and high-κ dielectrics. Phys Scr. 2013;88(6):068503. https://doi.org/10.1088/0031-8949/88/06/068503

27. Lomb NR. Least-squares frequency analysis of unequally spaced data. Astrophys Space Sci. 1976;39:447-462. https://doi.org/10.1007/BF00648343
28. Vilão RC, Vieira RBL, Alberto HV et al. Muonium donor in rutile TiO2 and comparison with hydrogen. Phys Rev B. 2015;92(8):081202(R). https://doi.org/10.1103/PhysRevB.92.081202
29. Alberto HV, Vilão RC, Piroto Duarte J et al. Hyperfine Interact. 2001;136-137:471-477. https://doi.org/10.1023/A:1020502219653
30. Pratt FL. Repolarization of anisotropic muonium in orientationally disordered solids. Philos Mag Lett. 1997;75(6):371-380. https://doi.org/10.1080/095008397179444
31. Houtepen AJ, Gil JM, Lord JS et al. Muonium in nano-crystalline II-VI semiconductors. Phys B 2009;404(5-7):837-840. https://doi.org/10.1016/j.physb.2008.11.158
32. Dalpian GM, Chelikowsky JR. Self-Purification in Semiconductor Nanocrystals. Phys Rev Lett. 2006;96(22):226802. https://doi.org/10.1103/PhysRevLett.96.226802
33. Chan TL, Tiago ML, Kaxiras E et al. Size Limits on Doping Phosphorus into Silicon Nanocrystals. Nano Lett. 2008;8(2):596-600. https://doi.org/10.1021/nl072997a